

How Topographic Slopes Control Gravity-spreading in Salt-bearing Passive Margins

Zhiyuan Ge^{1,1,1}, Matthias Rosenau^{2,2,2}, and Michael Warsitzka^{3,3,3}

¹China University of Petroleum, Beijing

²Helmholtz Center Potsdam - GFZ German Research Center for Geosciences

³Institute of Geophysics of the Czech Academy of Sciences

November 30, 2022

Abstract

Sediment progradation and spreading is a key process during gravity-driven, thin-skinned deformation in salt-bearing passive margins. However, to what degree the size and shape of a progradational sedimentary wedge control gravity-driven deformation is still not clear. We use analogue modelling to compare two endmember configurations constrained by critical wedge theory, in which the sediment wedge has different initial depositional slopes: a 5° critical (stable) slope and a 27° unstable slope. In both configurations, differential loading initiates spreading characterized by a basinward migrating system of linked proximal extension and distal contraction with a translational domain in between. With a critical frontal slope, the translational domain expands as the contractional domain migrates forward with viscous flow evenly distributed. With a steep frontal slope, both extensional and contractional domains migrate at similar rate due to more localized viscous flow under the wedge toe producing diagnostic structures of late extension overprinting early contraction. In both cases, salt flow is dominated by Poiseuille flow with only a subordinate contribution from Couette flow, contrasting to classical gravity gliding systems dominated by Couette flow. Comparison with previous studies reveal similar structural styles and viscous flow patterns. Our study highlights the geometric variations of sedimentary wedges result in variable responses in gravity spreading systems. With a steep frontal slope, the sediment wedge is more likely to collapse and develop spreading associated structures. However, such steep slope systems may not be very common in salt-bearing passive margins as they are less likely to occur in nature.

This manuscript is a preprint and has been submitted for peer review process. This manuscript has not been accepted or undergone proof read. Subsequent versions of this manuscript may have different content. Please feel free to contact any of the authors directly. We welcome feedback!

How Topographic Slopes Control Gravity Spreading in Salt-bearing

Passive Margins: Insights from Analogue Modelling

Zhiyuan Ge^{1,2,3}, Matthias Rosenau⁴ and Michael Warsitzka⁵

¹ State Key Laboratory of Petroleum Resources and Prospecting, China University of Petroleum (Beijing), Beijing, 102249, China.

² College of Geosciences, China University of Petroleum (Beijing), Beijing, 102249, China.

³ Department of Earth Science, University of Bergen, Allégaten 41, 5007 Bergen, Norway.

⁴ Helmholtz Centre Potsdam – GFZ German Research Centre for Geosciences, 14473 Potsdam, Germany

⁵ Institute of Geophysics of the Czech Academy of Sciences, Boční II/1401, 141 31 Prague 4, Czech Republic

Corresponding author: Zhiyuan Ge (gezhiyuan@cup.edu.cn)

Abstract

Sediment progradation and spreading is a key process during gravity-driven, thin-skinned deformation in salt-bearing passive margins. However, to what degree the size and shape of a progradational sedimentary wedge control gravity-driven deformation is still not clear. We use analogue modelling to compare two endmember configurations constrained by critical wedge theory, in which the sediment wedge has different initial depositional slopes: a 5° critical (stable) slope and a 27° unstable slope. In both configurations, differential loading initiates spreading characterized by a basinward migrating system of linked proximal extension and distal contraction with a translational domain in between. With a critical frontal slope, the translational domain expands as the contractional domain migrates forward with viscous flow evenly distributed. With a steep frontal slope, both extensional and contractional domains migrate at similar rate due to more localized viscous flow under the wedge toe producing diagnostic structures of late extension overprinting early contraction. In both cases, salt flow is dominated by Poiseuille flow with only a subordinate contribution from Couette flow, contrasting to classical gravity gliding systems dominated by Couette flow. Comparison with previous studies reveal similar structural styles and viscous flow patterns. Our study highlights the geometric variations of sedimentary wedges result in variable responses in gravity spreading systems. With a steep frontal slope, the sediment wedge is more likely to collapse and develop spreading associated structures. However, such steep slope systems may not be very common in salt-bearing passive margins as they are less likely to occur in nature.

1 Introduction

Gravity-driven tectonic deformation has been widely observed in salt-bearing passive margins (e.g. Allen et al., 2016; Brun and Fort, 2011; Fort et al., 2004; Peel, 2014; Rowan, 2020; Rowan et al., 2004; Vendeville, 2005) (Fig. 1). As the sediment progrades and deforms under its own weight above a basal evaporite layer, a typical linked system occurs with a zone of proximal extension and a corresponding zone of distal contraction (e.g. Dooley et al., 2020; Fort et al., 2004; Rowan et al., 2004). Despite sharing some common features, the gravity-driven failures usually display vast variations of structural styles and associated basin evolution, such as those basins along the south Atlantic margins and the neighboring basins in the east Mediterranean (Kukla et al., 2018; Zucker et al., 2019). The variations are largely due to the multiple controls involved in the gravity-driven deformation, from tectonics-induced deformation occurring in the whole basin to local sediment-structure interactions (Howlett et al., 2020; Ings et al., 2004; Rowan, 2020). Most controls can be attributed to one of the two basic modes of gravity-driven deformation: 1. gravity gliding driven by the tilting of the detachment layer (Fig. 1a); 2. gravity spreading associated with the collapse of a progradational sediment wedge due to differential loading (Fig. 1b) (Brun and Fort, 2011; Peel, 2014; Rowan et al., 2004; Schultz-Ela, 2001). For example, thermal subsidence and tectonic uplift contribute the gravity gliding, and sediment progradation and retrogradation affect gravity spreading (Rowan, 2020; Rowan et al., 2004).

Various criteria exist in defining gravity-driven deformation. Peel (2014) proposes the release of potential energy as the criteria to categorize gravity deformation as gravity gliding releases energy by slope parallel movement and gravity spreading release energy by deforming internally. The two types of viscous flow, namely the Couette and Poiseuille flows, have been thought to be associated with gravity gliding and gravity spreading, respectively (Brun and Fort, 2011; Gemmer et al., 2005). However, using salt flow analysis, Weijermars and Jackson (2014) address the frequent coexistence of Couette and Poiseuille flows in salt and, thus, the difficulty in distinguishing gliding and spreading during gravity-driven deformation.

We here follow the definition proposed by Raillard et al. (1997), which directly links the boundary conditions in analogue modelling with different modes of deformation: basin tilting and sediment progradation control gravity gliding and gravity spreading, respectively. However, even under such definition, there are different views on whether or how gravity spreading dynamics can dominate a gravity-driven salt tectonic system (e.g. Brun & Fort, 2011; Rowan et al., 2012). The ability of gravity gliding in controlling salt tectonics has been relatively well studied. Analogue modelling studies show that margin tilting alone is sufficient to drive pronounced gravity gliding with typical structural styles of upslope extension and downslope contraction (Brun and Fort, 2011; Cobbold and Szatmari, 1991; Dooley et al., 2020; Ge et al., 2019a; Quirk et al., 2012). In contrast, gravity spreading systems show considerable variations in structural style and basin evolution. For instance, progradational wedges can form expulsion rollovers or extensional grabens under different boundary conditions (Ge et al., 1997; McClay et al., 1998; Vendeville, 2005).

Analogue and numerical modelling studies have been focused on the influences of various controls, including progradation rate, sedimentation pattern, sediment transport direction as well as base-salt relief, on gravity spreading systems (Cohen and Hardy, 1996; Ge et al., 1997; Gemmer et al., 2005; Krézsek et al., 2007; McClay et al., 2003; McClay et al., 1998; Vendeville, 2005). However, little attention has been given to how geometric variation of sedimentary wedges affect a gravity-spreading system. In general, sedimentary progradational systems and their deposit are simplified and simulated as wedge-shaped sediment cover (e.g. Cohen & Hardy, 1996; Ge et al., 1997; Krézsek et al., 2007; McClay et al., 1998), with loosely defined sedimentological meanings. For example, the progradational rate and thickness of a sedimentary wedge are based on the interpolation of overall sediment cover thickness from a few sites in the basin (e.g. Adam et al., 2012; McClay et al., 1998). Even when specified with some sedimentological implications, variable frontal slope, which directly links the sedimentary wedge shape and associated depositional systems, have not been explicitly explored (e.g. Ge et al., 1997; Gemmer et al., 2005; Gradmann et al., 2009).

In this study, using analogue modelling, we investigate the structural and kinematic evolution of a passive margin salt tectonic system driven solely by progradation of sedimentary wedges. We hypothesize that a geometric variation in the frontal slope impose an important boundary condition. Wedge geometry has an effect on the force balance and the spreading dynamics of progradational wedges similar to accretionary wedges (e.g. Mourgues et al., 2014) which is often analysed in the framework of the critical coulomb wedge (or taper) theory (CWT, e.g. Dahlen, 1990). Based on sedimentological constrains, we here focus on two wedge geometries, one with a critically stable and another with an extensionally unstable frontal slope according to CWT. Moreover, we apply salt flow analysis on the results to infer the salt flow kinematics (e.g. Warsitzka et al., 2018) and include previous models with various frontal slopes into our analysis. Our models demonstrate how geometric variation of the progradational wedge is able to control the dynamics of a thin-skinned gravity-spreading system. The results shed lights on some issues of gravity-spreading systems in passive margins and provide additional application of critical taper theory and salt flow analysis to salt tectonics in general.

2 Materials and Methods

2.1 Geometric implication of sedimentary wedges

Sedimentary systems in passive margins have complex sedimentological and geomorphological features controlled by tectonics, basin morphonology, climate, sediment supply and so on (Carvajal et al., 2009; Helland-Hansen et al., 2012; O'Grady et al., 2000; Patruno and Helland-Hansen, 2018). In both physical and numerical simulations, sedimentary systems have been modelled as a sedimentary wedge thinning from proximal to distal with relatively smooth topographical slopes (Brun and Fort, 2011; Ge et al., 1997; Gemmer et al., 2005; Gradmann et al., 2009; Krézsek et al., 2007; McClay et al., 2003; Vendeville, 2005). In natural passive margin basins, sedimentary wedges typically have thicknesses of a few 100s to 1000s of metres (Carvajal et al.,

2009; Helland-Hansen et al., 2012; Patruno and Helland-Hansen, 2018), resulting in typical natural depositional slopes of $<5^\circ$ (Carvajal et al., 2009; O'Grady et al., 2000; Prather et al., 2017). However, in some cases, depositional slopes can be much steeper and close to the local angle of repose. Sea level changes, tectonics, and carbonate deposition can cause local slopes up to 30° (Prather et al., 2017; Ross et al., 1994; Schlager and Camber, 1986). In the northern Gulf of Mexico, for instance, some of the seafloor profiles crossing the salt-related structures show slopes of up to 20° (Lugo-Fernández and Morin, 2004; Roberts et al., 1999). At a smaller scale, Gilbert-type deltas usually have subaqueous slopes between $20\text{--}27^\circ$ (Nemec, 1990). Therefore, the natural sedimentary systems seem to be characterised by two types of depositional slopes: the gentle ones ($< 5^\circ$) and steep ones ($>5^\circ$, up to 30°), whereas the first type plays a dominant role in continental margins (O'Grady et al., 2000).

2.2 Constraints from Critical Wedge Theory (CWT)

According to CWT, a stability criterion (criticality) can be defined for a brittle wedge (with surface slope angle α) pushed along a detachment horizon (with dip angle β), which is a function of its geometry or “taper” angle ($\alpha+\beta$), the (effective) basal and internal strengths as well as the densities of the solid and pore fluid phases (e.g. Dahlen, 1990). In contrast to purely frictional wedges, we here constrain the basal strength from the observed shear rates and the silicone viscosity to be very low and equivalent to an effective friction angle of $<1^\circ$. Furthermore, we consider the detachment horizon to be horizontal ($\beta=0$) in our models.

Plotting the stability criterion into a α vs. β diagram results in a stability field and enclosed by a failure envelope, which represents the critical state geometry (Fig 2). Geometries plotting above the envelope are extensionally unstable while geometries below are contractionally unstable. Both wedges presented here tend to deform until the critical geometry representing force balance is reached. From a static point of view, any wedge slope above a viscous layer tends to relax to a very low taper ($<1^\circ$) due to the low long-term strength of the viscous substratum (Davis & Engelder, 1985). In a dynamic system, such as realized in the presented study, the deformation is continuously driven by sediment progradation. Hence, the geometric evolution is disturbed continuously.

Applying CWT suggests that gentle slopes of sedimentary wedge ($\sim 5^\circ$) are just at or slightly beyond the verge of failure (i.e. in the critical state), whereas steep slopes ($20\text{--}30^\circ$) are clearly in the extensionally unstable regime (Fig. 2a). Since the distance to the stability envelope is proportional to the force imbalance, we consider the two scenarios as representing endmembers of close to stable (or critical) and highly unstable wedges collapsing under extension.

2.3 Experimental setup and procedure

To test the effect of wedge stability on spreading dynamics, we use an analogue modelling approach that simulates complex salt tectonic evolution similar to previous studies (e.g. Brun & Fort, 2011; Ge et al., 2019a, b; McClay et al., 1998; Vendeville,

2005). We use a mixture of quartz sand and foam glass spheres as the cover material to achieve a reasonable density ratio of 1.16 between brittle and viscous layers (see Table 1). The brittle behaviour of this granular mixture (Warsitzka et al., 2019), is similar to sands used in previous analogue modelling studies (e.g. Klinkmüller et al., 2016) and to natural rocks (e.g. Byerlee, 1978). As an analogue of viscous salt, the silicone used in this study (KORASILON G30M) behaves like a Newtonian fluid up to a strain rate of about 10^{-2} s^{-1} , which is well beyond our experimental range (Rudolf et al., 2016). We derive a geometric scaling ratio of 10^{-5} (i.e. 1 cm in the model \approx 1 km in nature) and a time scaling ratio of $\sim 10^{-10}$ (i.e. 4 hours in the model \approx 1 Ma in nature) based on standard scaling procedures for submarine salt tectonic systems (see Adam and Krezsek, 2012 and references within) (Table 1).

A basal sand body on top of a rigid basal plate forms the mould of two identical silicone basins (Fig. 3). Compared to a setup with an even thickness silicone, the double-wedge shape of the silicone base is a more realistic representation of a passive margin salt basin (Brun and Fort, 2011; Zwaan et al., 2021). We note that the variation in silicone thickness may lead, besides velocity variations, to spatial strength variations within the viscous silicone. However, stability analysis shows that a spatial (or temporal) variation of even one order of magnitude in basal strength has little impact upon the stability fields (Fig. 2).

We test two syn-kinematic sedimentary wedges. Initially, the first model has a critical slope of roughly 5° (Model 1) and the second model has a steep, unstable slope of roughly 27° (Model 2). Both models start with sieving an even, 1 mm thick, pre-kinematic sand layer over the silicone before further sedimentation is added (Fig. 3a). Every 12 hours over a duration of 5 days, a maximum of 4 mm (Model 1) and 25 mm (Model 2) are added (fig. 3a) to simulate syn-kinematic sediment progradation. For simplicity, no lateral variations of sedimentation are considered.

Both wedges prograde basinward at the same rate of 10 cm day^{-1} ($\sim 10 \text{ km in 6 Ma}$) with an aggradational rate of 2 mm day^{-1} ($\sim 200 \text{ m in 6 Ma}$) (Fig. 3a), falling into the slower end of natural progradational systems (e.g. Carvajal et al., 2009). Due to constant progradational and aggradational rate, the frontal slope decreases to 2.6° in Model 1 and increases to 34.2° in Model 2 towards the end of the experiment (Fig. 3a). Thus, the stability analysis is still valid for both wedges during the experiment, although the actual frontal slope may vary slightly due to sieving more sand in topographically low areas (Fig. 2a). The variation of the progradational rate of the two wedges represents two types of sedimentary system as the one in Model 1 has a relatively stable shelf edge near the upslope basin boundary and the one in Model 2 has a fast migrating shelf edge. Thus, the different geometries of the two wedges also reflect the variable amounts of sediment input (Fig. 3).

During the experiment, the model surface is monitored with a stereoscopic pair of cameras. Digital image correlation (DIC; LaVision Davis 8, see details in Ge et al., 2020) applied on the stereoscopic images provides the 3D topography as well as incremental displacement (or velocity) and strain fields of the model surface at high spatial and temporal resolution (e.g. Adam et al., 2005). After the experiment, the

models are wetted, sequentially sliced, and photographed to provide cross-sectional views.

2.4 Silicone flow analysis

Based on the surface deformation derived from the DIC, we calculate the flow velocity field in the underlying silicone layer. We assume that the progradating sand wedge induces (1) a Poiseuille channel flow in the viscous layer driven by lateral differential loading (Fig. 4) and the resulting hydraulic head gradient (dP/dx) (Hudec and Jackson, 2007; Kehle, 1988). The hydraulic head gradient consists of the components of the pressure head gradient, produced by lateral changes of the sand layer thickness on top of the silicone, and the elevation head gradient, caused by lateral changes in the elevation of the top silicone. Furthermore, we suggest that the collapsing, basinward sliding wedge causes horizontal shear stresses, which linearly decrease with depth in the viscous layer inducing (2) a Couette shear flow component (Gemmer et al., 2005). Based on steady-state solutions of the Navier-Stokes equation, we derive the horizontal velocity u_x , consisting of flow components, by the following equation (e.g. Turcotte and Schubert, 2014 as applied in Warsitzka et al., 2018):

$$u_x = \frac{1}{2\eta} \frac{dP}{dx} (h_s^2 - z^2) + \frac{u_T}{h_s} \quad (\text{Eq. 1})$$

Here, η is the dynamic viscosity, h_s is the thickness of the silicone layer, z is the depth, and u_T is the horizontal velocity at the top of the silicone layer. For simplicity, we consider only the horizontal x -component of the hydraulic head gradient and the flow velocity, which is reasonable when the viscous layer is not tilted during the deformation. This computation bares the limitations that no deformation or strength of the cover layer was included, which would tend to reduce flow velocities. Therefore, the amounts of velocity calculated in our models are effectively the upper limits for cases when no shear strength acts. Furthermore, the flow velocity fields illustrated here should be considered instantaneous with no reflection of the dynamic redistribution (advection) of the silicone (Warsitzka et al., 2018).

As geometric input, simplified shapes of the experimental layers are used based on the DIC-derived digital topography (Fig. 4). We calculate the velocity for each phase, after adding a new sand layer, which modifies the topography and, therefore, the hydraulic head gradient. The downslope horizontal and the vertical DIC-derived surface velocity components v_x and v_z are then used to calculate the translation of the overburden, assuming that v_x at the top of the sand cover is equal to u_T at the base of the cover. The vertical velocity component v_z is transferred to the top silicone interface by an angle of 60° assuming that the overburden subsidence is translated to the base of the cover by 60° -dipping normal faults (cf. Fig. 3). During the computation procedure, the model is built with a grid of equidistant nodes (~ 1.5 mm distance). Then, the hydraulic head gradient is calculated between each node and inserted into the equation of the flow velocity u_x together with the measured velocity u_T (Eq. 1). Finally, the velocity field is smoothed to filter out small-scale topographic irregularities.

3 Experimental observations

3.1 Model 1: Progradation With Critical Depositional Slope

In Model 1 (5° critically stable slope), the input of sand cover wedge immediately triggers extension (Fig. 2a) occupying $\sim 10\%$ of the basin length (% b.l.) and contraction affecting $\sim 20\%$ b.l. with a translational domain of $\sim 20\%$ b.l. in between (Figs 5a & 6a). The extensional domain is characterised by two grabens (G1 and G2) while the contractional domain is composed of numerous small-wavelength (1–2 cm) folds and thrusts (F1) (Figs 5a & 6a). After 24 hours, as the sand wedge progrades basinward, an additional graben G3 occurs at 5 cm offset from G2, and an additional fold set (F2) nucleates 5 cm away from F1 (Fig 3a). Simultaneously with the development of new extensional and contractional structures, the translational domain (TD) increases to $\sim 30\%$ b.l. as a part of the contractional domain gets buried and becomes deactivated (Fig. 5a & 6a). Meanwhile the TD continues to spread reaching $>50\%$ b.l. by the end of the experiment (Fig. 5a & 6a). As the translational domain expands, the extensional domain increases to $>20\%$ b.l. until G1 deactivates after 72 hours (Fig. 6a). In contrast, the contractional domain decreases to $\sim 10\%$ b.l. after 64 hours until a new fold and thrust set F3 nucleates 10 cm offset from F2 (Fig. 6a). Contemporaneously with the occurrence of F3, a distal contractional structure F5 localizes at the basinward edge of the silicone basin, switching from its early extensional nature (Fig. 6a). A final migration of the contraction occurs at 84 hours as the fold and thrust set F4 develops c. 8 cm next to F3 (Fig. 6a).

3.2 Model 1: Progradation With Unstable Depositional Slope

In Model 2 (27° unstable slope), the sand wedge initiates three extensional grabens (G1–G3) and a small-wavelength fold and thrust set (F1) covering $\sim 10\%$ b.l. and $\sim 15\%$ b.l., respectively, with a translational domain (TD1) in between occupying $<5\%$ b.l. (Fig. 5b & 6b). In contrast to Model 1, no deformation occurs in the most landward area as spreading is localized at the wedge front (Fig. 6b). After 24 hours, a new extensional graben occurs between the initial translational domain (TD1) and the contractional domain, increasing the extensional domain to $\sim 15\%$ b.l. (Fig. 6b). Another fold and thrust set F2 forms in the basinward side of F1, followed by F3–F5 between 24–36 hours, increasing the contractional domain to $\sim 40\%$ b.l. (Fig. 6b). During the basinward migration of both domains, the early translational domain (TD1) is overprinted by the extensional domain, while the fold and thrust set (F1) becomes part of the new translational domain (TD2) (Fig. 6b). At 36 hours, contractional structures (F7) localize in the basinward basin edge (Fig. 6b). Around the 60-hour mark, an extensional graben (G5) occurs at the location of F2 and F3 while a distal contractional structure F6 also emerges (Fig. 6b). As a result of such markedly synchronous migration of the extensional and contractional domains, the translational domain (TD3) shifts again to the area between F3 and F4 (Fig. 6b). In the landward area, the extensional structures G1–G4 gradually deactivate and only G5 remains active at the end of the experiment (Fig. 6b). A final shift of the translational domain occurs at around 108 hours as F4 starts to extend and the area between F4 and F5 becomes part

of the translational domain (TD4) (Fig. 6b). Throughout the experiment, the successive, short lived translational domains of Model 2 occupy a relatively small and constant area (<5 % b.l.), compared to the long lived, expanding translational domain in Model 1 (>50 % b.l.).

3.3 Velocity and flow analysis

In both models, the surface velocity is extracted and averaged over the longitudinal profiles across the silicone basins. The measured surface velocity shows a local peak every time when new sediments are added in the experiment (Fig. 7a). As Model 2 receives more sediments, the surface velocity is also higher. However, although the sieved sediment increases gradually in both models (Fig. 2a), the averaged surface velocity reaches its peak between 30 and 60 hours and then gradually decreases until the end of the experiment (Fig. 7a).

Cross sectional views of the velocity patterns in the silicone layer derived from the flow analysis demonstrate that the Poiseuille (channel) flow (e.g. Weijermars & Jackson, 2014) dominate in both models, whereas Couette (shear) flow is subordinate (Fig. 8). This is also reflected by the average flow velocities of both components (Fig. 7b) showing that the Poiseuille flow u_p is always higher than the Couette flow component u_c . These results imply that the flow in the viscous layer is dominantly driven by differential loading and less by shearing related to the laterally moving cover wedge. Nevertheless, spatial differences in flow patterns can be observed between the two models. The flow field is widely distributed in Model 1 while localized under the frontal slope in Model 2 (Fig. 8). As the sediment wedge progrades, the flow field expands with the wedge in Model 1, but migrates forward following the frontal slope in Model 2. The averaged flow velocities reveal that the Couette flow component v_c is highest between 40 and 60 hours in both models (Fig. 7a), similar to the measured surface velocities (Fig. 7a). In contrast, the Poiseuille flow velocity u_p reaches its peak after 80 hours in both Model 1 and 2 (Fig. 7b), when the sand wedge gradually progradates over the area where the silicone layer is thickest.

4 Discussion

4.1 Wedge dynamics

Our experiments highlight how the spreading dynamics of critically stable vs. unstable progradational wedges control the structural style and kinematic evolution of gravity-driven deformation in salt basins. The main problem regarding the role of gravity spreading in salt tectonics is rooted in the question of whether it is alone a sufficient driver for thin-skinned deformation (Brun and Fort, 2011; Rowan et al., 2012). Consequently, identifying gravity spreading in nature becomes a key to solve the problem. One of the main diagnostic features of gravity spreading is the development of late extension over early contraction, as both domains migrate basinward along with the progradational wedge (Brun and Fort, 2011; McClay et al., 1998; Vendeville, 2005). Our Model 2, with a steep, unstable depositional slope, exemplifies such archetypical synchronicity (Fig. 7b). In contrast, with a gentle depositional slope in Model 1, the

gravity spreading system is more decoupled and characterized by long lived, expanding extensional and translational domains and a migrating contractional domain.

The kinematic evolution of Model 1 is notably similar to gravity-gliding systems driven by progressive margin tilting, where the actively deforming extension and contraction domains are separated by a relatively wide translational domain with little internal deformation (Ge et al., 2019a; their fig. 4). However, the flow field analysis shows that flow patterns in Model 1 are different from those in gravity gliding systems. The latter are generally dominated by Couette flow (Brun and Fort, 2011), whereas in our models Poiseuille flow exceeds the Couette flow component (Fig. 7b). This indicates that horizontal redistribution of the viscous substratum and vertical displacement of the cover dominates over lateral translation of the cover wedge and shearing of the viscous layer (Vendeville, 2005). Temporal changes of the displacement velocities (Fig. 7) suggest that the influence of both processes varies during different stage of the wedge progradation. The horizontal surface and Couette velocities culminate during the first half of the experiment and gradually decrease afterwards (Fig. 7). The Poiseuille flow velocity constantly increases and peaks in the second half of the experiment. We suggest that this temporal variation of the velocities is associated with the geometry of the silicone basin. Poiseuille flow velocity is generally higher, if the viscous layer is thicker (Eq. 1), as the effects of boundary drag are reduced. Thus, u_p is highest, where the wedge slope is the thickest within the silicone basin (Fig. 8). Consequently, Poiseuille flow accelerates as the wedge progrades basinward. And the pure shear deformation (“squeezing flow”; Weijermars & Jackson, 2014) in the viscous layer becomes more effective than simple shear deformation, which is equivalent to Couette shear flow. In another word, a larger proportion of the potential energy of the wedge is translated into vertical subsidence (squeezing of the viscous layer) instead of lateral translation, where the viscous layer becomes thicker.

The flow velocity also reveals the reason why the two wedges in Model 1 and 2 behave so differently. The flow velocity in Model 2 is significantly higher than Model 1, which results in a faster evacuation of the silicone beneath the frontal slope (Fig. 8b). Thus, the overburden wedge welds quickly on the base of the silicone locking upslope parts of the wedge and forcing the extensional and contractional domains to migrate downslope. In contrast, the slow expulsion of silicone in Model 1 causes a long-lasting deformation throughout the wedge and a relatively slow basinward migration of the extensional domain (Fig. 7a). Consequently, the translational domain expands continuously as the sand wedge propagates, resulting in a basin-wide deformation zone (Fig. 7a).

4.2 Comparison with other wedge-driven gravity spreading models

Numerous modelling studies have focused on the gravity spreading processes associated with sedimentary wedges (e.g. Adam and Krezsek, 2012; Brun and Fort, 2011; Ge et al., 1997; McClay et al., 2003; McClay et al., 1998; Vendeville, 2005; Yu et al., 2021). Although the results of these models, including the ones in this study, can

be qualitatively compared, a quantitative comparison among them are rather difficult due to various boundary conditions applied and modelling apparatus used. Our wedge stability and silicone flow analysis allow a quantitative comparison between all models. However, most published models do not provide surface velocity and deformation data. Thus, the CWT and flow analysis shown here are snapshots of the wedge stability with only Poiseuille flow component present (Figs 2b & 9). Furthermore, material properties (e.g. density, angle of internal friction) are not always specified. Therefore, we assume that materials commonly used in salt tectonic experiments are also used in these studies: silicone as salt analogue (viscosity: 10^4 Pas) and quartz sand as cover (bulk density: 1600 kgm^3).

In models by McClay et al. (1998; cf. their figure 3), the frontal slope was $<5^\circ$ at the beginning and increased to $>10^\circ$ due to continuous sand progradation and aggradation. Similar steep slopes of the progradational wedges were applied in models by Yu et al. (2021; cf. their figure 6), but in combination with an initially tilted silicone base. The models of both studies plot deeply in the extensionally unstable field in the CWT diagram (Fig. 2b). Similar as our Model 2, zones of high-velocity Poiseuille flow occur underneath the wedge front, whereas the cover already welds on the silicone base in landward regions (Fig. 9a and b). Sequential cross sections in Yu et al. (2021) display progressive seaward migration of the extensional domain and deactivation of landward extensional structures in the late stage of the models. Thus, such evolution of the deformation structures may be characteristic for gravity spreading systems with steep-slope wedges.

In contrast, models by Ge et al. (1997; cf. their figure 6) and Vendeville (2005; cf. their figure 6) applied relatively gentle slopes of roughly 5° , which plot at or close to the critical state envelope in the CWT diagram (Fig. 2). Consequently, the silicone flow is distributed evenly underneath the wedge (Fig. 9c and d), which is similar to the flow patterns in our Model 1 (Fig. 8). Restored cross sections in Vendeville (2005; cf. their figure 6) indicate that the most landward extensional structures remain active until late stage of the experiment while expanding seaward. Such deformation style seems to be typical for gentle-slope spreading systems as it can also be observed in our Model 1.

4.3 Comparison with nature

The two models presented here represent two endmembers of sediment-driven gravity spreading systems, which can be compared to natural prototypes. The Levant Basin in the eastern Mediterranean show typical features of a low-angle wedge propagating over the Messinian salt layer (Cartwright and Jackson, 2008). The restoration demonstrates that the sedimentary wedge had a front slope between $2.3\text{--}2.5^\circ$ from late Pliocene to present day (Fig. 10a). A relatively long (c. 20 km) translational domain developed between the proximal extension and the distal contraction (Cartwright & Jackson, 2008; their figure 9). Such a structural evolution is resembled by the one observed in our Model 1 (Fig. 7a). However, the Levant margin also went through a mild tilting of 0.5° . Thus, the gravity-spreading system might have been

slightly overprinted by gravity gliding and the salt flow may also vary through time (Evans and Jackson, 2020).

As a contrasting example the strata in the “Albian Gap” (the Cabo Frio area), located in the northern Santos Basin (Brazil), are characterised by basinward migrating extension, with early extensional rafts being tens of kilometers away from the late extension (Fig. 10b) (Pichel and Jackson, 2020). Such kinematic evolution is similar to the migration of extension from G4 to G5 in Model 2 (Fig. 7b), suggesting a high-angle frontal slope scenario. Basin physiographic analysis shows that the slope of the sedimentary wedges is up to 10° in the Cabo Frio area (Berton and Vesely, 2016), much steeper than the surrounding area where the current slope is generally $< 1^\circ$ (Henriksen et al., 2011).

In most cases, sedimentary progradational systems comprise various depositional slopes and sediment supply varies through space and time (Carvajal et al., 2009; Helland-Hansen et al., 2012; Henriksen et al., 2011). Furthermore, the associated sedimentary wedges have curved topographic slopes rather than straight ones (Adams and Schlager, 2000; Helland-Hansen et al., 2012). These progradational systems tend to have characteristics of both endmembers during their evolution. Moreover, although the two natural cases presented above show typical features of gravity spreading, other factors, such as margin tilting, basin geometry, and base-salt relief may still locally or temporarily affect the deformation pattern of the sedimentary wedges during their evolution (Dooley et al., 2020; Pichel & Jackson, 2020). Even when dominated by gravity spreading, spatial and temporal variations other than wedge geometry may also play important roles in controlling the deformation. For example, as the direction of sediment progradation is oblique to the (basinward) salt flow direction, the extension and contraction driven by sediment wedge may superimpose on the deformation parallel to the salt flow direction, forming complex salt-related structures (Guerra & Underhill, 2012) or basin-scale transfer zones (Brun & Fort, 2018).

5 Conclusions

We use an analogue modelling approach to provide an assessment of the role of gravity spreading controlled by variably steep progradational wedges in passive margin salt tectonics. Our experimental results suggest that a gravity-spreading system with a gentle frontal slope (close to stability in terms of force balance) is characterized by an expanding extensional domain, an increasing translational domain, and basinward migration of the contractional domain complemented with a more evenly distributed salt flow across the basin. Such a basin evolution shares kinematic similarities with gravity gliding systems that are driven by progressive margin tilting. In contrast, a spreading system with a steep, mechanically unstable frontal slope induces migrating extensional and contractional domains with a succession of translational domains resulting in a diagnostic structural pattern. The salt flow is more localized beneath the frontal slope of the wedge resulting in rapid salt welding and locking of the upslope parts of the wedge. In both cases, salt flow is dominated by Poiseuille flow with only a subordinate contribution from Couette flow thus in contrast to classical gravity gliding

systems characterized by Couette flow. The Poiseuille flow increases gradually as the wedge progrades to the basin centre where the silicone is thicker. Comparison with other gravity spreading dominant systems with various topographic slopes shows similar structural styles and silicone flow pattern. The two models presented in this study are endmembers of gravity spreading systems. Natural cases may show hybrid characters depending on the wedge stability. Other factors, such as margin tilting, salt thickness and base-salt relief may further complicate the deformation. Our study has important implications in interpreting thin-skinned salt tectonic deformation. For example, the downward migration of the extensional domain hints to a steep slope system, as it can be observed in the Santos Basin. However, such steep slope systems may not be very common in salt-bearing passive margins compare to their gentle slope counterparts due to their less likely occurrence in sedimentary systems.

Acknowledgments

ZG thanks the Science Foundation of China University of Petroleum, Beijing (No. 2462020QNXZ002) and L. Meltzers Høyskolefond for financial support. Frank Neumann and Thomas Ziegenhagen are thanked for technical assistance. We thank Nadaya Cubas for providing the script of the CWT analysis. We thank Jonathan Bedford for reading an early draft of this paper. GFZ Data Services are thanked for making the data openly accessible.

Experimental data of this study will be published open access in Ge et al. (2021): temporary preview link: <https://dataservices.gfz-potsdam.de/panmetaworks/review/297eadbaf7749a95ba2805adcd7602081bf9bceef5fbbc5afc423f43810f0058/>

References

- Adam, J., Z. Ge, and M. Sanchez, 2012, Post-rift salt tectonic evolution and key control factors of the Jequitinhonha deepwater fold belt, central Brazil passive margin: Insights from scaled physical experiments: *Marine and Petroleum Geology*, v. 37, p. 70–100.
- Adam, J., and C. Krezsek, 2012, Basin-scale salt tectonic processes of the Laurentian Basin, Eastern Canada: insights from integrated regional 2D seismic interpretation and 4D physical experiments: *Geological Society, London, Special Publications*, v. 363, p. 331–360.
- Adam, J., J. L. Urai, B. Wieneke, O. Oncken, K. Pfeiffer, N. Kukowski, J. Lohrmann, S. Hoth, W. van der Zee, and J. Schmatz, 2005, Shear localisation and strain distribution during tectonic faulting—new insights from granular-flow experiments and high-resolution optical image correlation techniques: *Journal of Structural Geology*, v. 27, p. 283–301.
- Adams, E. W., and W. Schlager, 2000, Basic Types of Submarine Slope Curvature: *Journal of Sedimentary Research*, v. 70, p. 814–828.

- Allen, H., C. A.-L. Jackson, and A. J. Fraser, 2016, Gravity-driven deformation of a youthful saline giant: the interplay between gliding and spreading in the Messinian basins of the Eastern Mediterranean: *Petroleum Geoscience*, v. 22, p. 340-356.
- Berton, F., and F. F. Vesely, 2016, Seismic expression of depositional elements associated with a strongly progradational shelf margin: northern Santos Basin, southeastern Brazil: *Brazilian Journal of Geology*, v. 46, p. 585-603.
- Brun, J.-P., and X. Fort, 2011, Salt tectonics at passive margins: Geology versus models: *Marine and Petroleum Geology*, v. 28, p. 1123-1145.
- Byerlee, J., 1978, Friction of rocks, *in* J. D. Byerlee, and M. Wyss, eds., *Rock friction and earthquake prediction: Contributions to Current Research in Geophysics (CCRG)*: Birkhäuser, Basel, Springer, p. 615-626.
- Cartwright, J. A., and M. P. A. Jackson, 2008, Initiation of gravitational collapse of an evaporite basin margin: The Messinian saline giant, Levant Basin, eastern Mediterranean: *Geological Society of America Bulletin*, v. 120, p. 399-413.
- Carvajal, C., R. Steel, and A. Petter, 2009, Sediment supply: The main driver of shelf-margin growth: *Earth-Science Reviews*, v. 96, p. 221-248.
- Cobbold, P. R., and P. Szatmari, 1991, Radial gravitational gliding on passive margins: *Tectonophysics*, v. 188, p. 249-289.
- Cohen, H. A., and S. Hardy, 1996, Numerical modelling of stratal architectures resulting from differential loading of a mobile substrate, *in* G. I. Alsop, D. J. Blundell, and I. Davison, eds., *Salt Tectonics*, v. 100, Geological Society, London, Special Publications, p. 265-273.
- Dooley, T. P., M. R. Hudec, L. M. Pichel, and M. P. A. Jackson, 2020, The impact of base-salt relief on salt flow and suprasalt deformation patterns at the autochthonous, paraautochthonous and allochthonous level: insights from physical models: Geological Society, London, Special Publications, v. 476.
- Evans, S., and C. A.-L. Jackson, 2021, Intracrustal Structure and Strain Partitioning in Layered Evaporites: Implications for Drilling Through Messinian Salt in the Eastern Mediterranean: *Petroleum Geoscience*, online first.
- Fort, X., J.-P. Brun, and F. Chauvel, 2004, Salt tectonics on the Angolan margin, synsedimentary deformation processes: *AAPG bulletin*, v. 88, p. 1523-1544.
- Ge, H., M. P. A. Jackson, and B. C. Vendeville, 1997, Kinematics and dynamics of salt tectonics driven by progradation: *AAPG bulletin*, v. 81, p. 398-423.
- Ge, Z., M. Warsitzka, M. Rosenau, and R. L. Gawthorpe, 2019a, Progressive tilting of salt-bearing continental margins controls thin-skinned deformation: *Geology*, v. 47, p. 1122-1126.
- Ge, Z., M. Rosenau, M. Warsitzka, and R. L. Gawthorpe, 2019b, Overprinting translational domains in passive margin salt basins: insights from analogue modelling: *Solid Earth*, v. 10, p. 1283-1300.
- Gemmer, L., C. Beaumont, and S. J. Ings, 2005, Dynamic modelling of passive margin salt tectonics: effects of water loading, sediment properties and sedimentation patterns: *Basin Research*, v. 17, p. 383-402.

- Gradmann, S., C. Beaumont, and M. Albertz, 2009, Factors controlling the evolution of the Perdido Fold Belt, northwestern Gulf of Mexico, determined from numerical models: *Tectonics*, v. 28.
- Helland-Hansen, W., R. J. Steel, and T. O. Sømme, 2012, Shelf genesis revisited: *Journal of Sedimentary Research*, v. 82, p. 133–148.
- Henriksen, S., W. Helland-Hansen, and S. Bullimore, 2011, Relationships between shelf-edge trajectories and sediment dispersal along depositional dip and strike: a different approach to sequence stratigraphy: *Basin Research*, v. 23, p. 3–21.
- Howlett, D., R. Gawthorpe, Z. Ge, A. Rotevatn, and C. A.-L. Jackson, 2021, Turbidites, Topography and Tectonics: Evolution of submarine channel-lobe systems in the salt-influenced Kwanza Basin, offshore Angola: *Basin Research*, v. 33, p. 1076–1110.
- Hudec, M. R., and M. P. Jackson, 2007, Terra infirma: Understanding salt tectonics: *Earth-Science Reviews*, v. 82, p. 1–28.
- Ings, S., C. Beaumont, and L. Gemmer, 2004, Numerical modeling of salt tectonics on passive continental margins: Preliminary assessment of the effects of sediment loading, buoyancy, margin tilt, and isostasy: *Perkins Research Conference*, p. 36–68.
- Kehle, R. O., 1988, The origin of salt structures, *in* B. C. Schreiber, ed., *Evaporites and Hydrocarbons*: New York, Columbia University Press, p. 345–404.
- Klinkmüller, M., G. Schreurs, M. Rosenau, and H. Kemnitz, 2016, Properties of granular analogue model materials: A community wide survey: *Tectonophysics*, v. 684, p. 23–38.
- Krézsek, C., J. Adam, and D. Grujic, 2007, Mechanics of fault and expulsion rollover systems developed on passive margins detached on salt: insights from analogue modelling and optical strain monitoring: *Geological Society, London, Special Publications*, v. 292, p. 103–121.
- Kukla, P. A., F. Strozyk, and W. U. Mohriak, 2018, South Atlantic salt basins – Witnesses of complex passive margin evolution: *Gondwana Research*, v. 53, p. 41–57.
- Lugo-Fernández, A., and M. M. Morin, 2004, Slope and Roughness Statistics of the Northern Gulf of Mexico Seafloor With Some Oceanographic Implications: *Gulf of Mexico Science*, v. 22.
- McClay, K., T. Dooley, and G. Zamora, 2003, Analogue models of delta systems above ductile substrates: *Geological Society London Special Publications*, v. 216, p. 411–428.
- McClay, K. R., T. Dooley, and G. Lewis, 1998, Analog modeling of progradational delta systems: *Geology*, v. 26, p. 771–774.
- Mourgues, R., A. Lacoste, and C. Garibaldi, 2014, The Coulomb critical taper theory applied to gravitational instabilities: *Journal of Geophysical Research: Solid Earth*, v. 119, p. 754–765.
- Nemec, W., 1990, Aspects of Sediment Movement on Steep Delta Slopes, *in* A. Colella, and D. Prior, eds., *Coarse-Grained Deltas*, *International Association of Sedimentologist Special Publication*, p. 29–73.

- O'Grady, D. B., J. P. M. Syvitski, L. F. Pratson, and J. F. Sarg, 2000, Categorizing the morphologic variability of siliciclastic passive continental margins: *Geology*, v. 28, p. 207–210.
- Patruno, S., and W. Helland-Hansen, 2018, Clinoforms and clinoform systems: Review and dynamic classification scheme for shorelines, subaqueous deltas, shelf edges and continental margins: *Earth-Science Reviews*, v. 185, p. 202–233.
- Peel, F., 2014, The engines of gravity-driven movement on passive margins: Quantifying the relative contribution of spreading vs. gravity sliding mechanisms: *Tectonophysics*, v. 633, p. 126–142.
- Pichel, L. M., and C. A. Jackson, 2020, The Enigma of the Albian Gap: Spatial Variability and the Competition Between Salt Expulsion and Extension: *Journal of the Geological Society*, v. 177, 1129–1148.
- Prather, B. E., C. O'Byrne, C. Pirmez, and Z. Sylvester, 2017, Sediment partitioning, continental slopes and base-of-slope systems: *Basin Research*, v. 29, p. 394–416.
- Quirk, D. G., N. Schødt, B. Lassen, S. J. Ings, D. Hsu, K. K. Hirsch, and C. Von Nicolai, 2012, Salt tectonics on passive margins: examples from Santos, Campos and Kwanza basins: *Geological Society, London, Special Publications*, v. 363, p. 207–244.
- Raillard, S., B. C. Vendeville, and G. Gue'rin, 1997, Causes and structural characteristics of thin-skinned inversion during gravity gliding or spreading above salt or shale, AAPG Annual Convention Official Program, p. A95.
- Roberts, H., R. McBride, and J. Coleman, 1999, Outer shelf and slope geology of the Gulf of Mexico: an overview: *The Gulf of Mexico Large Marine Ecosystem*: Blackwell Science.
- Ross, W., B. Halliwell, J. May, D. Watts, and J. Syvitski, 1994, Slope readjustment: a new model for the development of submarine fans and aprons: *Geology*, v. 22, p. 511–514.
- Rowan, M. G., 2020, Salt- and shale-detached gravity-driven failure of continental margins: *Regional Geology and Tectonics* (Second Edition).
- Rowan, M. G., F. J. Peel, and B. C. Vendeville, 2004, Gravity-driven fold belts on passive margins, *in* K. R. McClay, ed., *Thrust tectonics and hydrocarbon systems*, AAPG Memoir, p. 157–182.
- Rowan, M. G., F. J. Peel, B. C. Vendeville, and V. Gaullier, 2012, Salt tectonics at passive margins: *Geology versus models—Discussion: Marine and Petroleum Geology*, v. 37, p. 184–194.
- Rudolf, M., D. Boutelier, M. Rosenau, G. Schreurs, and O. Oncken, 2016, Rheological benchmark of silicone oils used for analog modeling of short-and long-term lithospheric deformation: *Tectonophysics*, v. 684, p. 12–22.
- Schlager, W., and O. Camber, 1986, Submarine slope angles, drowning unconformities, and self-erosion of limestone escarpments: *Geology*, v. 14, p. 762–765.
- Schultz-Ela, D. D., 2001, Excursus on gravity gliding and gravity spreading: *Journal of Structural Geology*, v. 23, p. 725–731.

- Turcotte, D., and G. Schubert, 2014, *Geodynamics* (3rd ed.): Cambridge, Cambridge University Press.
- Vendeville, B. C., 2005, Salt tectonics driven by sediment progradation: Part I—Mechanics and kinematics: *AAPG bulletin*, v. 89, p. 1071–1079.
- Warsitzka, M., Z. Ge, J.-M. Schönebeck, A. Pohlenz, and N. Kukowski, 2019, Ring-shear test data of foam glass beads used for analogue experiments in the Helmholtz Laboratory for Tectonic Modelling (HelTec) at the GFZ German Research Centre for Geosciences in Potsdam and the Institute of Geosciences, Friedrich Schiller University Jena, GFZ Data Services.
- Warsitzka, M., N. Kukowski, and J. Kley, 2018, Salt flow direction and velocity during subsalt normal faulting and syn-kinematic sedimentation—implications from analytical calculations: *Geophysical Journal International*, v. 213, p. 115–134.
- Weijermars, R., and M. P. Jackson, 2014, Predicting the depth of viscous stress peaks in moving salt sheets: Conceptual framework and implications for drilling: *AAPG bulletin*, v. 98, p. 911–945.
- Yu, Y., C. Tao, S. Shi, J. Yin, C. Wu, and J. Liu, 2021, Physical modeling of salt structures in the middle south Atlantic marginal basins and their controlling factors: *Petroleum Exploration and Development*, v. 48, p. 136–145.
- Zucker, E., Z. Gvirtzman, J. Steinberg, and Y. Enzel, 2019, Salt tectonics in the Eastern Mediterranean Sea: Where a giant delta meets a salt giant: *Geology*, v. 48, p. 134–138.
- Zwaan, F., M. Rosenau, and D. Maestrelli, 2021, How initial basin geometry influences gravity-driven salt tectonics: Insights from laboratory experiments: *Marine and Petroleum Geology*, p. 105195.

Figure and table caption

Figure 1. (a) Gravity gliding vs. (b) gravity spreading systems (modified after Allen et al., 2016). Both deformation modes are generally associated with a landward extension and a seaward shortening as well as lateral redistribution of the salt.

Figure 2. Wedge stability analysis using Critical Wedge Theory (CWT) (Dahlen, 1990). (a) The two wedge geometries applied in our study and various wedge geometries of previous studies are plotted together with the CWT predicted stability fields. The two curves correspond to viscous strength equivalent basal friction angles of 0.1° and 1° (red = 0.1° , green = 1°) representing the expected range of basal strength. (b) Zoom into the CWT model domain.

Figure 3. Cross-sectional (a) and plane view (b) of the model design. A gentle-slope wedge ($\sim 5^\circ$) is applied in Model 1 and a steep-slope wedge ($\sim 27^\circ$) in Model 2.

Figure 4. Schematic diagram of flow analysis based on the setup of the presented analogue experiments. The sand wedge on top of the silicone layer induces a

Poiseuille channel flow (u_p). Due to the redistribution of the silicone, the sand wedge collapses gravitationally, which means it subsides into the silicone layer and slides laterally. The lateral sliding with the velocity u_T causes a Couette shear flow component (u_c) overlapping with the Poiseuille flow.

Figure 5. Map views of incremental longitudinal surface strain (ϵ_{xx}) in Model 1 (a) and 2 (b) at early (9–10 h), intermediate (49–50 h) and late (89–90 h) stages during the experiment.

Figure 6. (a) Middle cross section and the associated longitudinal surface strain rate map of Model 1. Note the expansion of extensional and translational domains as well as the basinward migration of the contractional domain. (b) Middle cross section and the associated longitudinal surface strain rate map of Model 2. Note the synchronized basinward migration of both extension and contraction and the shifts of the translational domain (TD). Strain rate maps are constructed by plotting strain rate (1 h increments) along the middle profile (x axis) over time (y axis).

Figure 7. (a) Surface velocity averaged profile vs. time for Model 1 and 2 along the middle section. The dashed lines represent the actually measured velocities derived from the DIC analysis, whereas the solid line is the moving average. (b) Average values of the Poiseuille flow u_p and Couette flow velocity u_c derived from the silicone flow analysis for each phase of sedimentation. In both models, Poiseuille flow dominates over Couette flow.

Figure 8. Representative cross sections showing the velocity field in the silicone and the cover layer from early (13–24 h), mid (37–48h) and late (61–72h) stages during model evolution. Silicone flow is widely distributed in Model 1, whereas it is focused beneath the frontal edge of the wedge in Model 2.

Figure 9. Representative cross sections of previous analogue modelling studies on gravity spreading showing the Poiseuille flow patterns in the viscous layer. Cross sections derived from the literature are used as input for the silicone flow analysis. (a) Flow patterns in the viscous layer based on cross sections of Model 1 and Model 2 in McClay et al. (1998). Poiseuille flow is fastest beneath the wedge front. (b) Flow patterns based on cross sections of two successive stage of Model 1 in Yu et al.(2021). The base of the silicone is tilted with 5° . (c) Flow patterns based on restored cross sections of two stage of Model 1 in Ge et al. (1997). Note the relatively even distribution of silicone flow beneath wedge in profile 1 and more localized flow in profiles 2. (d) Flow patterns based restored cross sections of the model shown in Vendeville (2005). Note the relatively even distribution of the viscous flow beneath the wedge.

Figure 10. (a) Cross section along the Levant margin in the eastern Mediterranean Sea. Note the translational domain in the mid slope and its overall similarity to Model 1 (modified from Fig. 9 in Cartwright & Jackson, 2008). (b) South–central section from the Albian Gap (the Cabo Frio Fault). Note the early and late (migrated)

extension and possible early contraction (modified from Fig. 7 in Pichel & Jackson, 2020).

Table 1. Material properties and scaling parameters of the experiments. Geometric scaling of 1cm in model is 1 km in nature. Time scaling of 1 h in model is 0.268 Ma in nature. For full details of the scaling, see (Adam et al., 2012).

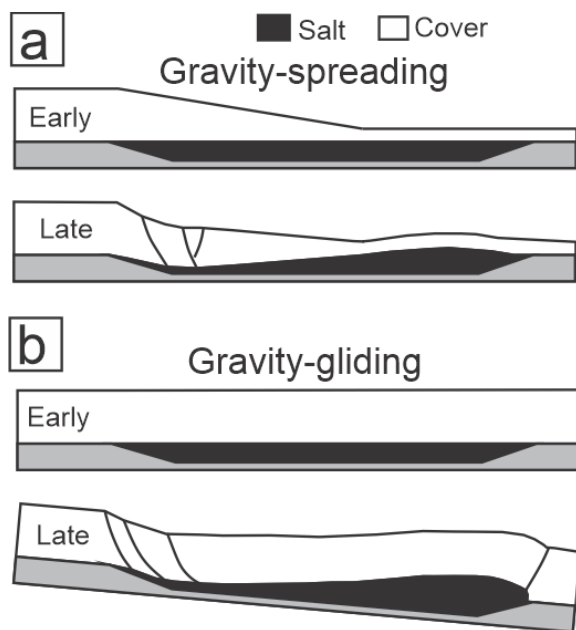


Figure 1

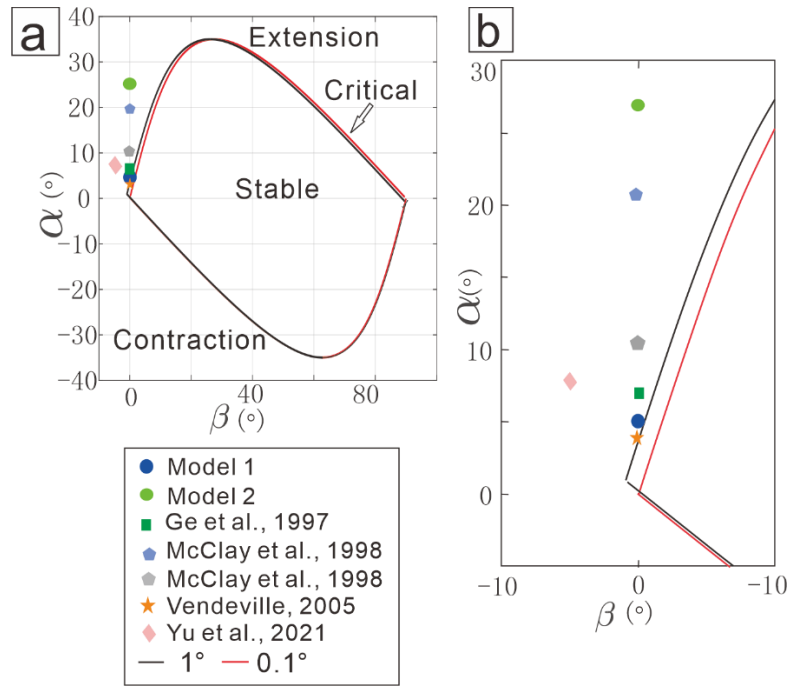


Figure 2

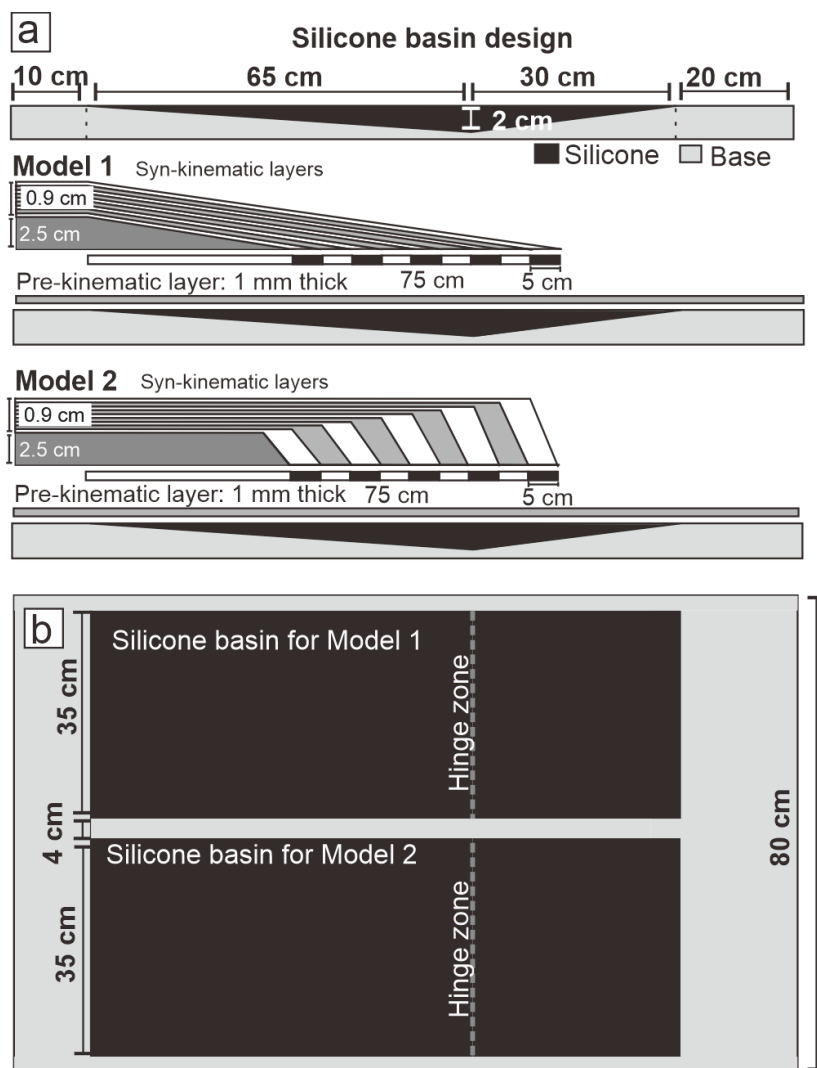


Figure 3

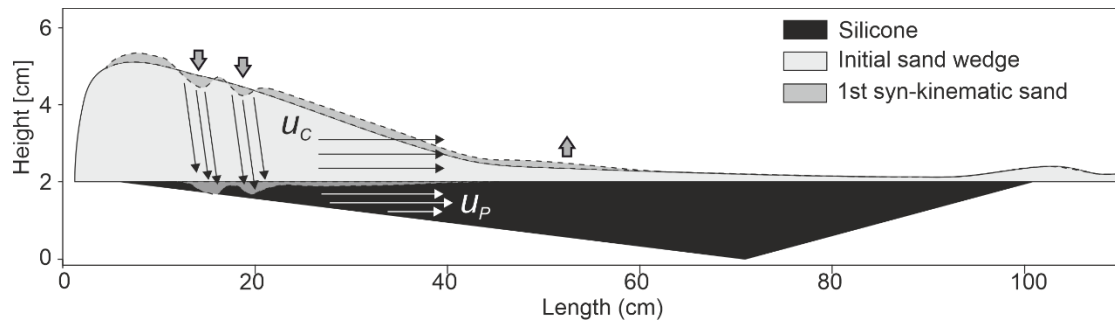


Figure 4

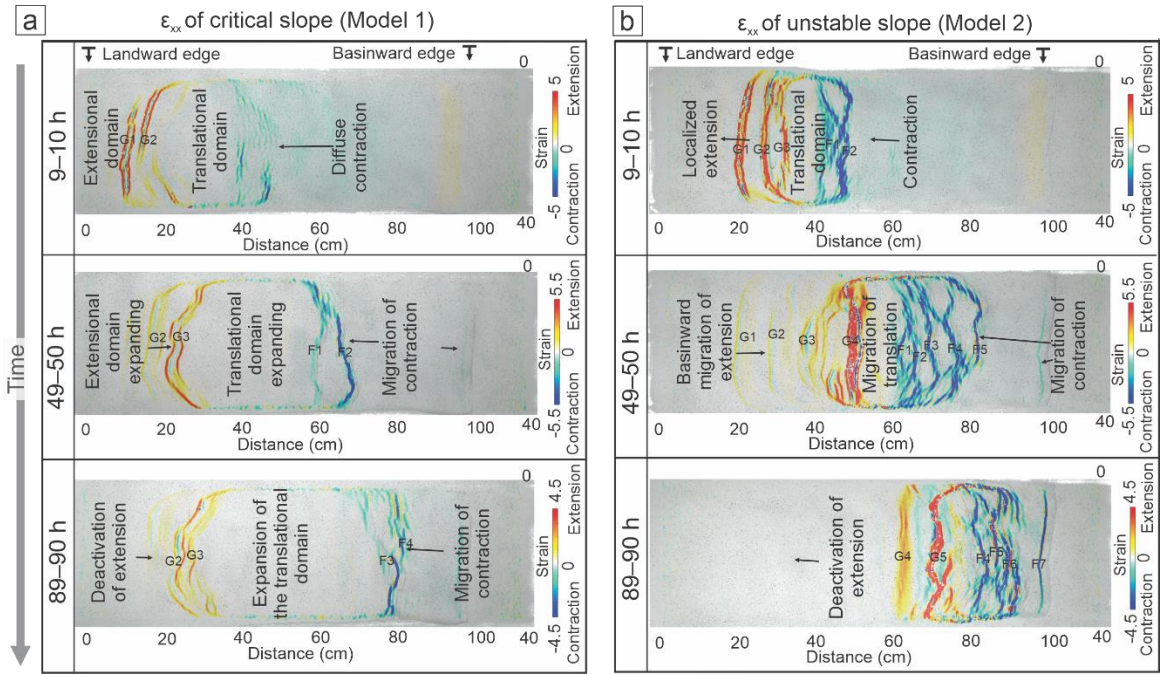


Figure 5

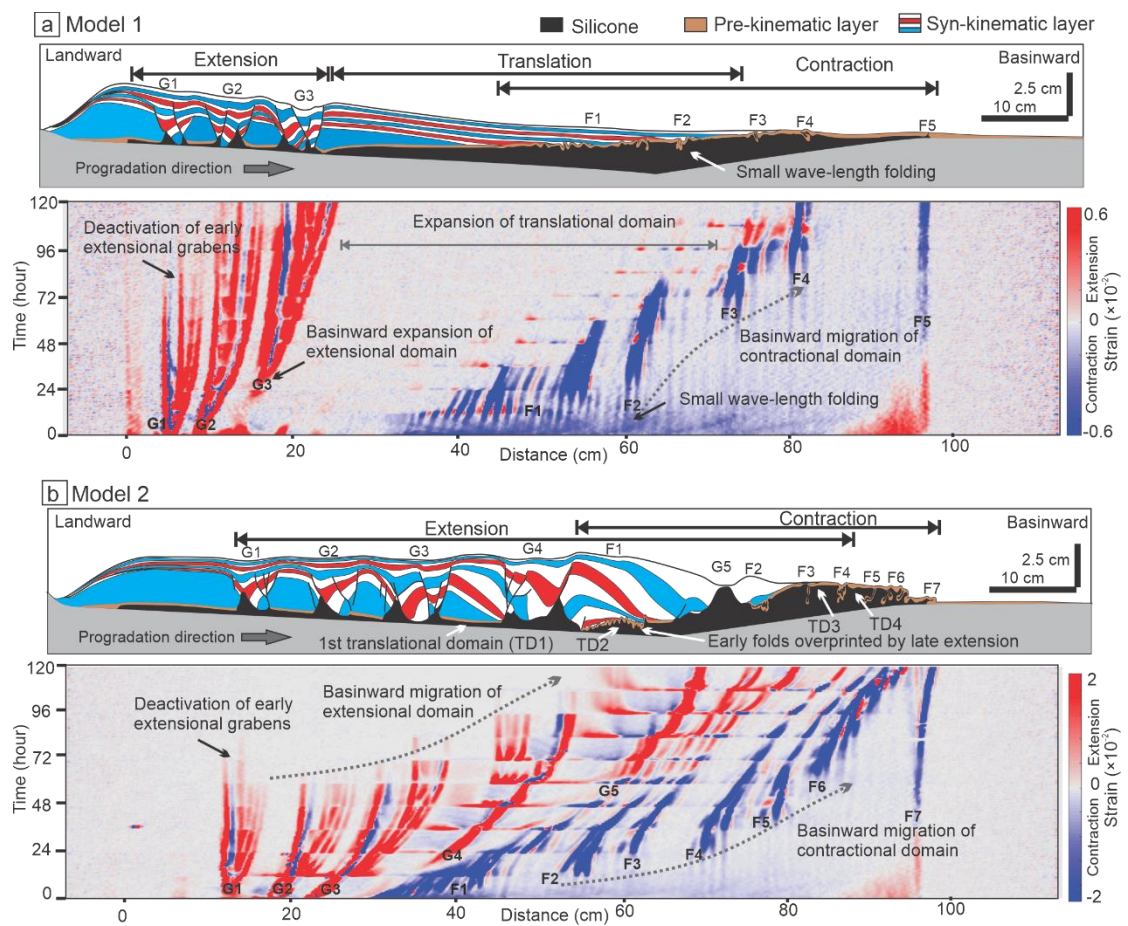


Figure 6

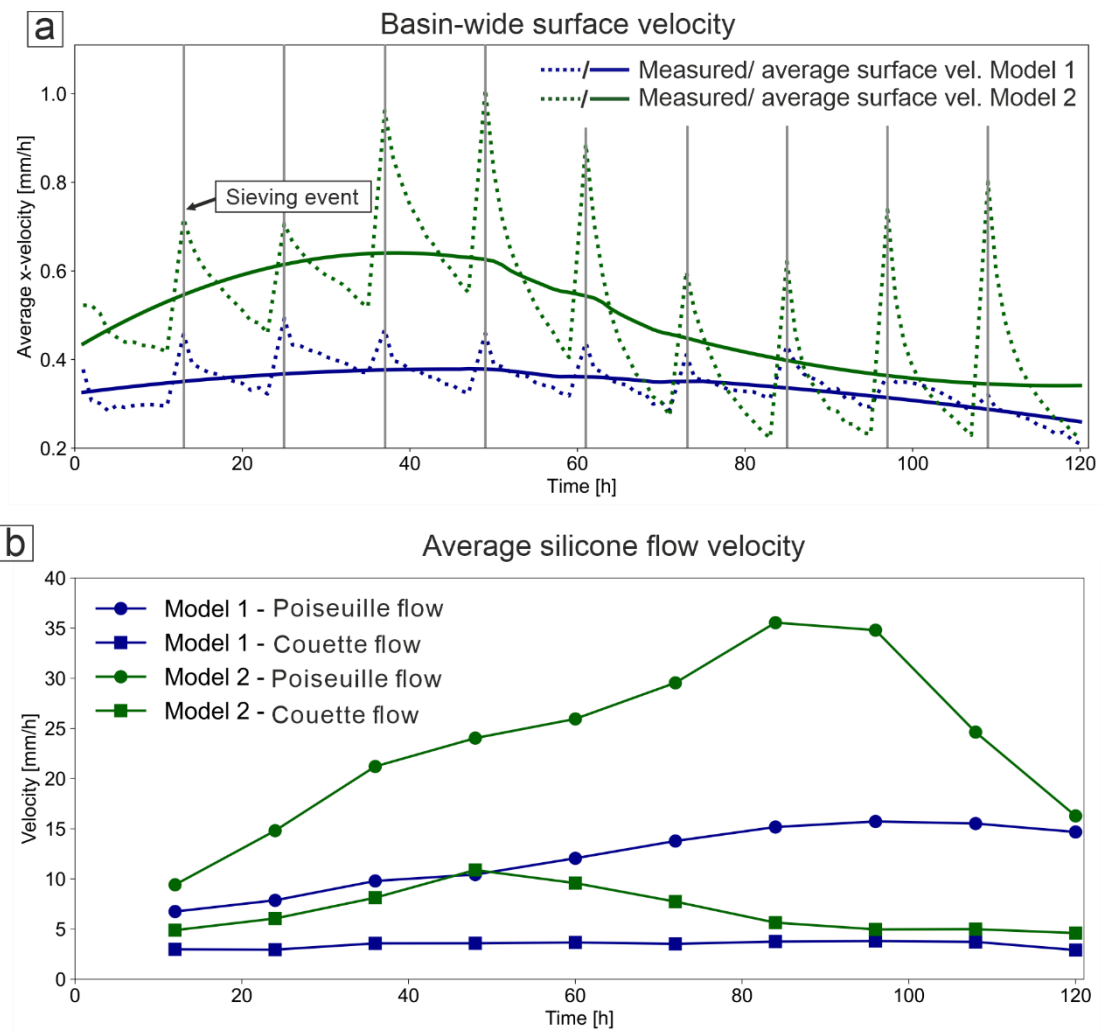


Figure 7

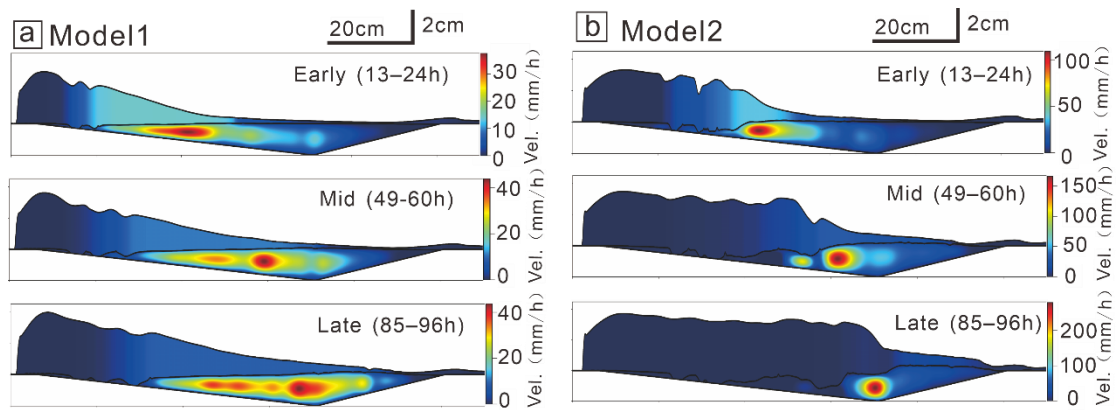


Figure 8

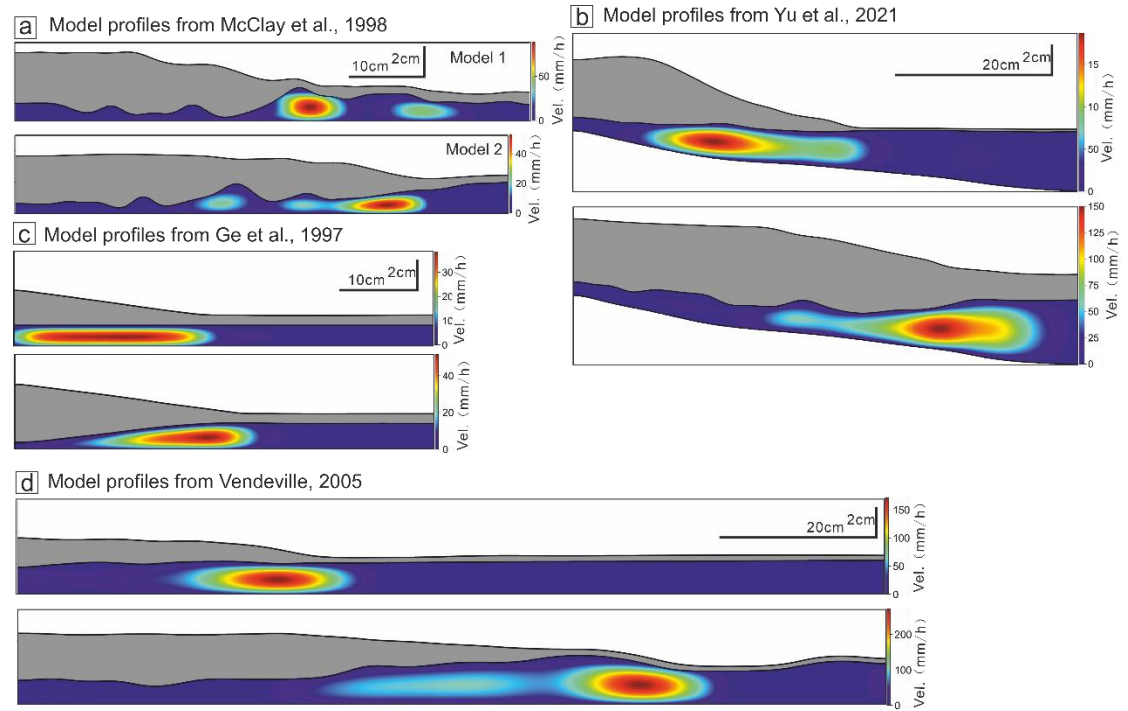


Figure 9

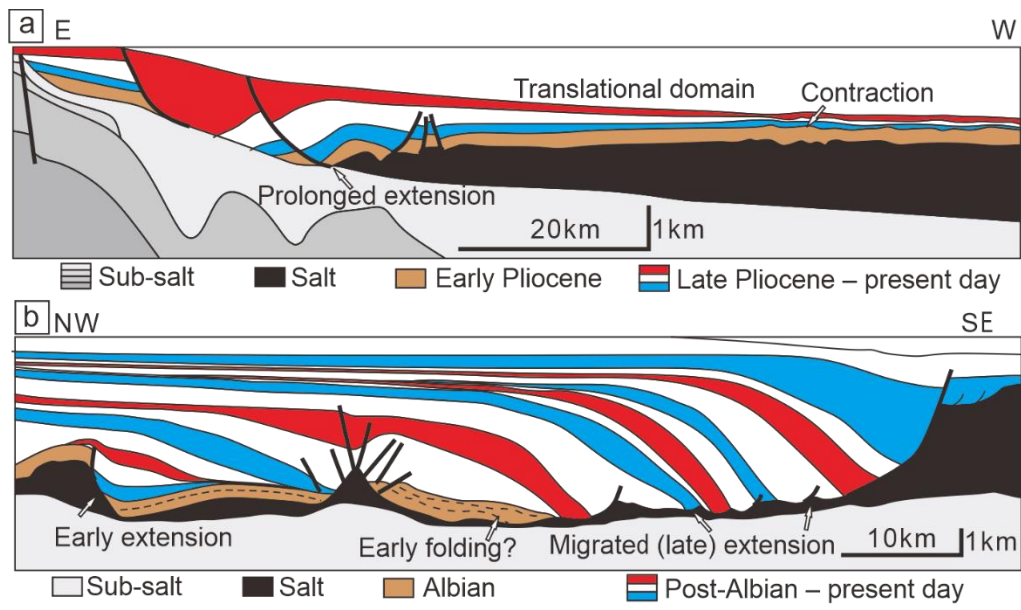


Figure 10

Scaling table:

Quantity	Symbol	Unit	Value (model)	Value (prototype)	Scaling relation	Scaling factor
Length	l	m	0.01	1	$l^* = l_{\text{model}}/l_{\text{prototype}}$	10^{-5}
Density overburden	ρ_c	$kg \cdot m^{-3}$	1130	2400	$\rho_c^* = \rho_{c \text{ model}}/\rho_{c \text{ prototype}}$	0.47
Gravity acceleration	g	$m \cdot s^{-2}$	9.81	9.81	$g^* = g_{\text{model}}/g_{\text{prototype}}$	1
Friction coefficient [#]	μ	-	0.55–0.75	0.40–0.80	$\mu^* = \mu_{\text{model}}/\mu_{\text{prototype}}$	1
Cohesion [#]	C	Pa	35–75	10^7	$C^* = \rho_c^* l^* g^*$	10^{-5}
Stress	σ	Pa	100 2.00	21.30×10^6	$\sigma^* = \rho_c^* l^* g^*$	4.70×10^{-6}
Viscosity*	η	$Pa \cdot s$	$\times 10^4$	5.00×10^{18}	$\eta^* = \eta_{\text{model}}/\eta_{\text{prototype}}$	4.00×10^{-15}
Strain rate	ϵ	s^{-1}	10^{-2} – 10^{-7}	10^{-11} – 10^{-16}	$\epsilon^* = \sigma^*/\eta^*$	1.18×10^9
Time (subaerial) Time (submarine)	t_a t_m	h h	1 1	1.18×10^9 2.35×10^9	$t_a^* = 1/\epsilon^*$ $t_m^* = 0.5 t_a^*$	8.51×10^{-10} 4.26×10^{-10}

[#]For static>reactivation>dynamic friction coefficients (Warsitzka et al., 2019)

*Viscosity after Rudolf et al. (2016)

742

743 Table 1